SPi	Journal Code				Article ID				Dispatch: 13.11.12	CE: Crystal Gayle M. Sarming
	P	I	P		2	3	2	5	No. of Pages: 15	ME:

PROGRESS IN PHOTOVOLTAICS: RESEARCH AND APPLICATIONS
Prog. Photovolt: Res. Appl. (2012)
Published online in Wiley Online Library (wileyonlinelibrary.com). DOI: 10.1002/pip.2325

RESEARCH ARTICLE

New explicit current/voltage equation for *p-i-n* solar cells including interface potential drops and drift/diffusion transport

Q2 Kurt Taretto*

Dto. de Electrotecnia, Univ. Nacional del Comahue-CONICET, Buenos Aires 1400, 8300 Neuquén, Argentina

UNCORRECTED PROOF

Q3 ABSTRACT

Analytical modeling of *p-i-n* solar cells constitutes a practical tool to extract electronic material and device parameters from fits to experimental data and to establish optimization criteria. This paper proposes a model for *p-i-n* solar cells based on a new approximation, which estimates the electric field taking into account interface potential drops at the intrinsic-to-doped interfaces. This leads to a closed-form current/voltage equation that shows very good agreement with device simulations, revealing that the inclusion of the interface potential drops constitutes a major correction to the classical uniform-field approach. Furthermore, the model is able to fit experimental current/voltage curves of efficient nanocrystalline Si and microcrystalline Si *p-i-n* solar cells under illumination and in the dark, obtaining material parameters such as mobility-lifetime product, built-in voltage, or surface recombination velocity. Copyright © 2012 John Wiley & Sons, Ltd.

KEYWORDS

p-i-n solar cell; drift-diffusion model; analytical $J(V)$ curve; ideality factor; surface recombination; interface recombination; nanocrystalline silicon; microcrystalline silicon; interface potential drop; band offset

***Correspondence**

Kurt Taretto, Dto. de Electrotecnia, Univ. Nacional del Comahue-CONICET, Buenos Aires 1400, 8300 Neuquén, Argentina.
E-mail: kurt_taretto@yahoo.com

Received 15 June 2012; Revised 5 September 2012; Accepted 22 October 2012

1. INTRODUCTION

To a large extent, the long-term success of a given material, layer system, or fabrication technique for solar cells is conditioned by the possibilities to understand the experimental data in terms of physical device models. This paper focuses on modeling *p-i-n* type solar cells, which are diodes based on an intrinsic layer (*i*-layer) placed between two thin *p*-type and *n*-type doped layers [1]. In *p-i-n* diodes used for photodetectors and solar cells, the *i*-layer is thin enough to establish a sufficiently strong field that efficiently drives the photogenerated charge carriers towards the device contacts [1,2]. Solar cells based on amorphous silicon (a-Si), nanocrystalline (nc-Si) and microcrystalline (μc-Si) silicon [1,3], organic compounds [4], and high-gap inorganic semiconductors [5] all use a *p-i-n* structure to maximize performance. The optimization of these solar cells towards higher efficiencies is primarily driven by characterization and modeling.

Modeling by numerical methods to solve simultaneously the highly nonlinear semiconductor continuity, transport and electrostatic equations are widely used and often provide physical insight and obtain a detailed picture of each studied solar cell [6–8]. However, the number of required parameters logically increases with the level of detail, and one is frequently confronted with the situation that several unknown parameters must be guessed. Analytical modeling tends to produce a more rudimental but often sufficient description of the device [9,10], requiring fewer parameters, and much less computing time in parametrical studies. In the case of *p-i-n* solar cells, analytical descriptions of the current/voltage characteristics are available when decoupling the electrical field from the transport equations [11], assuming a constant electric field [12] and additionally neglecting diffusion currents [12–15]. The inclusion of diffusion currents seems however mandatory to obtain meaningful device descriptions at voltages near the maximum power point and beyond [16–19]. Uniform field approaches still enable explicit solutions, typically assuming that the equilibrium field is given by V_{bi}/d, where V_{bi} is the built-in voltage and d is the *i*-layer thickness. This implicitly neglects the potential

Copyright © 2012 John Wiley & Sons, Ltd.

drop at the interfaces between the doped layers and the *i*-layer, which tends to overestimate the actual value of the field, requiring smaller *n/p*-layer doping values than the actual values in order to fit $J(V)$ measurements [17]. Additionally, it is shown here that neglecting the interface potential drops leads to strong overestimations of the effect of surface recombination.

The present work develops an analytical model for the current density (J)/voltage (V) characteristics of *p-i-n* solar cells taking into account drift and diffusion currents and assuming a constant electric field in the *i*-layer. A key feature of the model is that the potential drops at the *p-i* and *i-n* interfaces are taken into account, yielding a uniform field that is smaller than V_{bi}/d. A convenient analytical equation describing the interface potential drops allows defining a simple equation for the electric field in the *i*-layer, enabling a straightforward solution of the minority carrier continuity equations. This leads to an analytical expression of the $J(V)$ curve of *p-i-n* cells that contains both the reduced electric field due to the interface potential drops and the incidence on effective surface recombination of the potential drops seen as minority carrier energy barriers.

In Section 2, the electrical model of the *p-i-n* solar cell is described along with the assumed simplifications, which yield particular solutions of the electrostatic and the carrier transport/recombination equations—and finally the current/voltage curve. Specific mathematical aspects are given in Appendices A and B. Section 3 tests, with the aid of device simulations, the ability of the model to predict solar cell current/voltage curves and solar output parameters over a range of different key parameters. In Section 4, the model is applied to experimental solar cell data of state-of-the-art nc-Si and µc-Si *p-i-n* solar cells, obtaining material parameters such as mobility-lifetime product, built-in voltage, and surface recombination velocity. The parameters extracted from the fits are then contrasted with data from the literature and discussed. Finally, Section 5 draws conclusions on the model, its limitations, and advantages.

2. MODEL

F1 Figure 1 schematically shows the energy band diagram of a homojunction *p-i-n* solar cell of thickness d under thermal equilibrium conditions, indicating the Fermi energy level E_F (dash-dotted line) and the valence/conduction band edges E_V/E_C, respectively (solid lines). The "shoulders" seen at the band edges in the limits of the *i*-layer reveal the potential drop at the *p-i* and *i-n* interfaces. The total energy difference between the front and back surfaces is indicated by qV_{bi}, where V_{bi} is the built-in potential fixed by the doping concentrations in the p and n layers. The dotted line (red online) in Figure 1 represents the simplest approximation to the actual band diagram, where the band edges are given by a straight line across the *i*-layer, neglecting any potential drop at the interfaces. Here, we define this approach as the mean field approximation, being the mean electric field given by

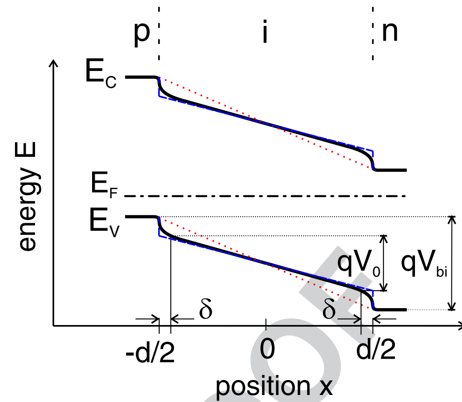

Figure 1. Energy band diagram of a *p-i-n* structure of thickness d under thermal equilibrium. The solid lines represent the actual conduction and valence band energies E_C and E_V, respectively, whereas the dash-dotted line represents the Fermi level. The potential difference across the junction is the built-in potential V_{bi}, whereas the potential drop inside the *i*-layer is V_0. The dotted line shows the mean-field approximation, which neglects the potential drop at the *p-i* and *i-n* interfaces, whereas the dashed lines show the approximation adopted in this work, which assumes interface potential drops.

Colour online, B&W in print

UNCORRECTED PROOF

$F_{mean} = -V_{bi}/d$. A more refined approach is obtained by considering the interface potential drops as in the case of the dashed lines (blue online) in Figure 1, resulting in a weaker yet constant electric field F_0 in the *i*-layer. This is the approach followed throughout this paper, and the next section develops the appropriate equations to estimate F_0.

2.1. Electric field

Poisson's equation formulated in the *i*-layer reads $d^2\psi(x)/dx^2 = q(n-p)/\varepsilon_s$ where $\psi(x)$ is the local electrostatic potential, x the position coordinate, q the elementary charge, p and n the hole and electron concentrations, respectively, and ε_s the absolute dielectric constant [2]. The thermal equilibrium carrier concentrations follow the Boltzmann expressions taking the Fermi level as reference, yielding $n = n_i \exp(\psi(x)/V_t)$ and $p = n_i \exp(-\psi(x)/V_t)$ [8], where $V_t = kT/q$ is the thermal voltage, k is Boltzmann's constant, and T the absolute temperature. Replacing these expressions of n and p in Poisson's equation, we obtain the so-called Poisson–Boltzmann equation for the electrostatic potential

$$\frac{d^2\psi(x)}{dx^2} = \frac{V_t}{L_i^2} \sinh\left(\frac{\psi(x)}{V_t}\right) \quad (1)$$

where $L_i = \sqrt{\varepsilon_s V_t/(2qn_i)}$ is the intrinsic Debye–Hückel length in the *i*-layer, which in intrinsic silicon at room temperature is $L_i \approx 24\,\mu\text{m}$. A first integration of Eq. (1) yields

Prog. Photovolt: Res. Appl. (2012) © 2012 John Wiley & Sons, Ltd.
DOI: 10.1002/pip

$$\frac{1}{2}\left(\frac{d\psi(x)}{dx}\right)^2 = \left(\frac{V_t}{L_i}\right)^2 \cosh\left(\frac{\psi(x)}{V_t}\right) + c \qquad (2)$$

being c an integration constant. Defining the electric field in the center of the i-layer by $F_0 = -d\psi(x)/dx|_{x=0}$, we obtain $c = F_0^2/2 - (V_t/L_i)^2$. The solution procedure for this equation is analogous to the problem of the ideal pendulum at arbitrary swing amplitude [20,21], only that we need to solve for the amplitude instead of the pendulum's period. Replacing c in Eq. (2) and taking the boundary condition $\psi(0) = 0$, the solution to Eq. (2) reads

$$\psi(x) = -2\mathrm{j}V_t \,\mathrm{am}\left(-\frac{\mathrm{j}F_0 x}{2V_t}, \left(\frac{2V_t}{F_0 L_i}\right)^2\right) \qquad (3)$$

where am(u,m) is Jacobi's amplitude function with argument u and phase m and $\mathrm{j} = \sqrt{-1}$, defined as the inverse elliptic integral of the first kind [22]. If we assume for simplicity that the potential profile is point-symmetric around $x = 0$, the built-in voltage by definition must satisfy $V_{bi} = \psi(d/2) - (-d/2) = 2\psi(d/2)$, and the unknown F_0 is given by the root to the equation

$$4\mathrm{j}V_t \,\mathrm{am}\left(\frac{\mathrm{j}F_0 d}{4V_t}, \left(\frac{2V_t}{F_0 L_i}\right)^2\right) - V_{bi} = 0 \qquad (4)$$

Figure 2 shows in solid lines the ratio F_0/F_{mean} with F_0 computed from Eq. (4), as a function of V_{bi}/V_t and d/L_i as the parameter. Evidently, one may incur large overestimations when assuming F_{mean} as the true field in the i-layer. For example, in a 2.4 μm thick i-layer ($d/L_i = 0.1$), with $V_{\mathrm{bi}} = 0.85$ V, we obtain $F_{\mathrm{mean}} = 3.5$ kV/cm, whereas F_0 reaches only $F_0 = 0.7 \times F_{\mathrm{mean}}$ (enter Figure 2 with $V_{\mathrm{bi}}/V_t = 35$). In organic solar cells, F_0 is clearly below F_{mean} too, because typically one finds $V_{\mathrm{bi}} > 0.9$ V, and thicknesses much smaller than L_i, a combination of parameters that leads to $F_0 < F_{\mathrm{mean}}$.

An explicit expression of F_0 is available by recognizing that in solar cells that satisfy $d/L_i < 1$ and $V_{\mathrm{bi}}/V_t >> 1$, a series expansion of Eq. (3) about $m = 0$ leads to an accurate approximation for the field in the i-layer (Appendix A). The resulting equation for F_0 is given by

$$F_0 \cong -\frac{4V_t}{d} \ln\left(\sqrt{2}\frac{V_{\mathrm{bi}}}{V_t}\frac{L_i}{d}\right). \qquad (5)$$

In Figure 2, the dotted lines are calculated with Eq. (5), which, compared with the "exact" solution shown by the solid lines, indicate that Eq. (5) gives F_0 with a maximum error of 10% in the displayed range of variables. In efficient silicon p-i-n cells where $30 < V_{\mathrm{bi}}/V_t < 40$ and with $d/L_i = 0.1$, the approximation error introduced in Eq. (5) is smaller than 2%.

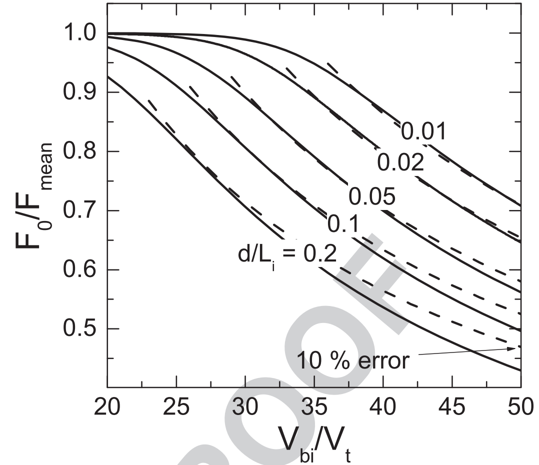

Figure 2. Relationship between the field F_0 in the center of the i-layer of a p-i-n junction and the mean field F_{mean} given by the quotient between built-in voltage V_{bi} and i-layer thickness d, as a function of the ratio V_{bi}/V_t, where V_t is the thermal voltage. The different curves are calculated with the indicated values of the ratio d/L_i, where L_i is the intrinsic Debye–Hückel length ($L_i = 24$ μm in silicon). Because of the potential drop at the p-i and i-n interfaces, the field F_0 may be substantially weaker than the mean field, depending on the thickness and built-in potential. The solid lines correspond to the exact solution computed by Eq. (4), whereas the dotted lines are calculated with the explicit expression Eq. (5).

Having the field F_0, the potential drop V_0 corresponding to the constant field region (Figure 1) can be approximated by

$$V_0 = |F_0|(d - 2\delta) \qquad (6)$$

where δ is the thickness of the regions where the interface potential drop develops, before reaching the constant field region where the potential varies linearly (Figure 1). An analytical expression for the distance δ is available by inspection of the first terms of the series expansion of Eq. (3) (appendix A), leading to

$$\delta \cong \frac{2V_t}{|F_0|} \qquad (7)$$

Next, we introduce the deviation from equilibrium by assuming that a bias potential V is applied between the extremes of the p-i-n junction. We consider the case where the forward bias injects majority carrier in the doped layers without exceeding the equilibrium concentrations, that is, low injection conditions. Under this situation, if we assume that the injected charge does not significantly modify the potential drop at the interfaces, the potential difference in the constant-field region is $V - V_0$, leading to a bias-dependent field in the i-layer given by

UNCORRECTED PROOF

$$F = \frac{V - V_0}{d} \quad (8)$$

This will be a good approximation up to voltages V approaching V_0 (F approaching zero). Above $V = V_0$, the charge injection into the *i*-layer is so high that any further applied potential will drop at the *p-i* and *i-n* interfaces.

In the next section, the field given by Eq. (8) is introduced in the transport equations to obtain the current/voltage characteristics. In previous models, this field was estimated by $F = (V - V_{bi})/d$, which may strongly overestimate the actual field in moderately thick devices or in devices with relatively high V_{bi}, leading to underestimated saturation current densities and overestimated open-circuit voltages under illumination.

2.2. Current/voltage equation

To obtain the current/voltage equation, we neglect the contributions from the much thinner *n* and *p* layers, leaving us with the problem of solving the carrier profile within the *i*-layer only. We make the following assumptions corresponding to the "symmetrical *p-i-n* solar cell":

1. identical mobilities μ for electrons and holes,
2. equal majority carrier concentration in *n* and *p* layers, identical front/back surface recombination velocities,
3. recombination rate linear with respect to the minority carrier concentration, with equal recombination lifetime τ for both carrier types,
4. uniform, that is, position-independent photogeneration rate.

These assumptions yield symmetrical carrier concentration profiles, meaning that the concentration of only one carrier type is needed to obtain the total current. Therefore, it is sufficient to formulate only the continuity equation for electrons in the first half of the *i*-layer according to Figure 1, where electrons are minorities, obtaining [2]

$$G - \frac{n(x) - n_0(x)}{\tau} + D\frac{d^2 n(x)}{dx^2} + \mu F \frac{dn(x)}{dx} = 0 \quad (9)$$

where $n_0(x)$ is the equilibrium electron concentration and D the diffusion constant, related to the carrier drift mobility by $D = V_t \mu$. Because a linearly varying band diagram is assumed, the equilibrium concentration in the *i*-layer is given by

$$n_0(x) = n_i \exp(V_0 x / V_t d) \quad (10)$$

Therefore, integrating Eq. (9), we obtain the solution where β_1 and β_2 are voltage-dependent parameters given by

$$\beta_{1,2} = \sqrt{\left(\frac{L}{d}\right)^{-2} + \left(\frac{V - V_0}{2V_t}\right)^2} \pm \left(\frac{V - V_0}{2V_t}\right) \quad (12)$$

with the plus sign belonging to β_1. The integration constants C_1 and C_2 in Eq. (11) are obtained applying the following two boundary conditions:

$$\text{I)}\ \ n\ (0) = n_i \exp(V/2V_t) \quad (13)$$

meaning that out of equilibrium, the quasi-Fermi levels in the center of the *i*-layer split by the applied voltage V. The conditions under which this is applicable were discussed in detail in Reference [17]. The second boundary condition

$$\text{II)}\ \ J_n(-d/2) = qS(n(-d/2) - n_0(-d/2)) \quad (14)$$

establishes that there is a current component that accounts for interface recombination at the *p-i* interface, that is, at $x = -d/2$, given by a recombination velocity S. The recombination velocity S must be interpreted as an effective recombination velocity that contains the effect of both, the recombination at the *p-i* and *i-n* interfaces and the recombination at the front/back surfaces.

The application of the boundary conditions I and II yields the integration constants C_1 and C_2 shown in Appendix B. Having the electron concentration $n(x)$ in the first half of the *i*-layer, we are able to compute the drift-diffusion current density in the center of the *i*-layer according to $J_n(0) = q\mu n(0)F + qDn'(x)|_{x=0}$. Because electron and hole parameters are assumed identical and the *p-i-n* cell is symmetric, the carrier concentration profiles are symmetric too, and therefore, the total current density J of the cell is equal to $J = 2J_n(0)$. Expressed as the sum of dark current and photocurrent density, this results in

$$J(V) = J_{\mathrm{dark}}(V) - J_{\mathrm{photo}}(V) \quad (15)$$

with the photocurrent given by

$$n(x) = G\tau + n_0(-d/2) \times \left(\frac{\exp(V_0 x / V_t d)}{1 - \frac{V_0 V L^2}{V_t^2 d^2}} + C_1 \exp(-\beta_1 x/d) + C_2 \exp(\beta_2 x/d) \right) \quad (11)$$

UNCORRECTED PROOF

Prog. Photovolt: Res. Appl. (2012) © 2012 John Wiley & Sons, Ltd.
DOI: 10.1002/pip

$$J_{\mathrm{photo}}(V) = qG\frac{2L^2}{d} \times \left\{ \left[\beta_2 + \frac{Sd}{D} + \left(\frac{V - V_0}{V_t} - \frac{Sd}{D}\right)\mathrm{e}^{-\beta_1/2}\right] \times A_1 - \beta_1 \right\} \tag{16}$$

where

$$A_1 = \frac{\beta_1 + \beta_2}{\beta_2 + \frac{Sd}{D} + \left(\beta_1 - \frac{Sd}{D}\right)\mathrm{e}^{-\frac{\beta_1+\beta_2}{2}}} \tag{17}$$

It can be shown that $0 < A_1 < 1$ for forward voltages that satisfy $V < V_0$. A necessary check of Eq. (16) for consistency is immediately possible by evaluating the limit of $J_{\mathrm{photo}}(V)$ at high reverse bias. Through all-analytical treatment of Eq. (16), the limit is found to be $J_{\mathrm{photo}}(V \to -\infty) = qGd$, which corresponds to the maximum photocurrent—constrained only by photogeneration and thickness.

The dark current density obeys

$$J_{\mathrm{dark}}(V) = \frac{2qn_iD}{d} \times \left[\left(\beta_1 + \frac{\frac{Sd}{D} - \beta_1}{\mathrm{e}^{\frac{\beta_1+\beta_2}{2}}}A_1\right) \times \left(\mathrm{e}^{\frac{V}{2V_t}} - \frac{1}{1 - \frac{V_0VL^2}{V_t^2d^2}}\right) + \frac{V}{V_t} \times \left(\frac{1 + A_2}{1 - \frac{V_0VL^2}{V_t^2d^2}}\right)\right] \tag{18}$$

being

$$A_2 = \left(1 + \frac{S\tau}{d}\frac{V_0}{V_t}\right) \times A_1\mathrm{e}^{-\frac{V_0}{2V_t} - \frac{\beta_1}{2}} \tag{19}$$

In Eq. (18), A_2 has been crossed suggesting that it can be safely neglected because in all practical cases, it will hold that $|A_2| << 1$.

It is possible to obtain a saturation current density J_0 by finding the limit of J_{dark} at large negative bias ($V \to -\infty$), resulting

$$J_0 = 2qn_i\left(\frac{dV_t}{\tau V_0} + S\exp\left(-\frac{V_{\mathrm{bi}}}{2V_t}\right)\right) \tag{20}$$

In most cases, the second term in the parenthesis turns negligible, leaving us with the expression $J_0 = 2qn_idV_t/(\tau V_0)$, which agrees with the equation of J_0 of previous drift-only models if we let $V_0 \to V_{bi}$.

2.3. Effective surface recombination velocity

Although formally the model assumes an effective recombination velocity S occurring at the *p-i* and *i-n* interfaces as seen from the *i*-layer, it is possible to relate S to the actual surface/interface recombination velocities. By surface, let us mean the back contact or metallization layer and the front transparent conductive layer. We notice that according to the band diagram of Figure 1, minority carriers need to surpass an energy barrier to reach the interfaces and surfaces. Therefore, it becomes evident that S is effectively related to the actual interface and surface recombination velocities S_{int} and S_{surf}, respectively.

The theory of back-surface fields in *pn* cells under low injection conditions allows to express the physical surface recombination velocity S_{surf} as an effective parameter evaluated at the edge of the space-charge region adjacent to the base of a back surface field junction, for example, at the edge of a back p-p^+ junction [23]. The effective surface recombination velocity is thus given by $S_{\mathrm{surf}} \times \exp(-\Delta E/kT)$, where ΔE is the band-edge step achieved across the p-p^+ junction. In the particular case of a homojunction p-p^+ interface, ΔE represents the energy barrier imposed by the built-in voltage of the p-p^+ junction. In our case of the *p-i-n* homojunction solar cell, in Figure 1, we see that under thermal equilibrium conditions, ΔE is given by $\Delta E = q(V_{bi} - V_0)/2$. Because the present model assumes that a low injection-applied voltage does not affect the voltage drop at the *p-i* and *i-n* interfaces, S is given by

$$S = (S_{\mathrm{int}} + S_{\mathrm{surf}})\exp\left(\frac{V_0 - V_{\mathrm{bi}}}{2V_t}\right) \tag{21}$$

Because the argument of the exponential term is always negative, we realize that the interface potential drops that weaken the field in the *p-i-n* cell have the beneficial effect of strongly reducing surface recombination. For the previous example of a silicon cell having $V_0/V_{bi} = 0.7$ and $V_{bi} = 0.85\,\mathrm{V}$, Eq. (21) predicts $S = 7 \times 10^{-3}(S_{\mathrm{int}} + S_{\mathrm{surf}})$. If we express the equilibrium field by Eq. (5) to obtain V_0 from Eq. (6), it is straightforward to obtain the approximated effective interface recombination velocity

$$S \approx 2(S_{\mathrm{int}} + S_{\mathrm{surf}})\left(\frac{L_iV_{\mathrm{bi}}}{dV_t}\right)^2\exp(-V_{\mathrm{bi}}/2V_t) \tag{22}$$

According to this equation, surface/interface recombination effects are effectively reduced in cells with high built-in voltages and high intrinsic layer thicknesses. This places a trade-off between higher thickness needed for both higher absorption and the virtual surface passivation provided by the interface potential drops and lower thickness needed for higher carrier collection and open-circuit voltage.

In heterojunction *p-i-n* solar cells where the *p* and *n* layers are made from a higher gap semiconductor, Eq. (21) must be rewritten including the band offsets corresponding to the minority carrier band that is relevant at the *p-i* or *i-n* interface under study. For the case of an *i-n* interface, we must

UNCORRECTED PROOF

consider the conduction band offset ΔE_C, obtaining the effective interface recombination velocity

$$S = (S_{\mathrm{int}} + S_{\mathrm{surf}}) \exp\left(\frac{V_0 - V_{\mathrm{bi}}}{2V_t} - \frac{\Delta E_C}{kT}\right) \qquad (23)$$

In the next section, Eq. (21) is introduced into the $J(V)$ curve to compare modeled versus numerically simulated $J(V)$ curves with front/back surface recombination. It will be shown that the model is able to predict the influence of surface recombination on the efficiency of homojunction *p-i-n* solar cell over a broad range of built-in voltages. Equation (23) will be needed further in the analysis of heterojunction *p-i-n* solar cell data.

3. COMPARISON TO SIMULATIONS

This section compares current/voltage curves for the case of a generic *p-i-n* solar cell obtained with the solar cell simulator PC1D5.1 with the corresponding modeled $J(V)$ curves. The numerical simulations were performed under two scenarios:

a) symmetric parameters and uniform generation rate G, that is, in full compatibility with the analytical approach, and
b) asymmetrical mobilities with a hole/electron mobility ratio of $\mu_p/\mu_n = 1/3$ and depth-dependent generation rate calculated by the simulator, assuming an AM1.5 G illumination spectrum with 100 mWcm^{-2} power density (corresponding to a spatial mean generation rate $7.3 \times 10^{20}\,\mathrm{cm^{-3}\,s^{-1}}$).

The simulations and the model share the following parameters: intrinsic carrier concentration $n_i = 10^{10}\,\mathrm{cm^{-3}}$, relative dielectric constant $\varepsilon = 11.9$, thermal voltage $V_t = 25.9\,\mathrm{mV}$, *i*-layer thickness $d = 2\,\mu\mathrm{m}$, and n and p layers doping $N_d = 10^{18}\,\mathrm{cm^{-3}}$, which yield $V_{\mathrm{bi}} = 0.95\,\mathrm{V}$ [2] and $V_0 = 0.58\,\mathrm{V}$, according to Eq. (6). The minority carrier recombination velocity at contacts is $S_{\mathrm{surf}} = 10^5\,\mathrm{cm\,s^{-1}}$, which in the analytical model is introduced by computing S according to Eq. (21) with $S_{\mathrm{int}} = 0$.

Recombination was simulated assuming Shockley–Read–Hall (SRH) defect recombination through a single defect energy level with equal capture cross sections placed at the intrinsic Fermi level, which yields recombination lifetimes equal to the band-to-defect transition times $\tau_{0,n/p}$, leading to $\tau_{n/p} = \tau_{0,n/p} = \tau$.

The values of carrier mobilities in the simulations were chosen to yield three possible values for the ambipolar diffusion lengths: $L = d/2$, $L = d$ or $L = 2d$, being L defined by

$$L = 2L_n L_p / \left(L_n + L_p\right) \qquad (24)$$

where $L_{n/p} = \sqrt{V_t \mu_{n/p} \tau_{n/p}}$. This allows a consistent comparison between the simulations with $\mu_n \neq \mu_p$ and the analytical model where $\mu_n = \mu_p = \mu$.

Figure 3 compares light $J(V)$ characteristics obtained by the simulator (symbols) and Eqs (15) through (18) given previously (lines), with the parameters given in Table I. The mobility values are combined with lifetime values that yield ambipolar diffusion lengths of either $L = d/2$ (diamonds, dotted line), $L = d$ (circles, crosses, solid and dash-dotted line) or $L = 2d$ (squares, dashed line). The baseline simulation corresponds to the case $L = d$, obtained with $\tau_n = \tau_p = 68\,\mathrm{ns}$ and $\mu_n/\mu_p = 50/15\,\mathrm{cm^2\,Vs^{-1}}$, which give the ambipolar mobility value $\mu = 2\mu_n\mu_p/(\mu_n + \mu_p) = 23\,\mathrm{cm^2\,Vs^{-1}}$.

Comparing the simulated and modeled curves in Figure 3, we notice that the analytical model reproduces accurately the $J(V)$ curves, except for the dash-dotted line, which was calculated using the mean-field approximation. For the baseline case with $L = d$, the resulting open-circuit voltage V_{OC} of the analytical model (solid line) exceeds the simulated V_{OC} (circles) by 4 mV. This difference is partly due to the assumed symmetry in the model, because the corresponding symmetric simulation (crosses in Figure 3) shows an only 1.5 mV smaller V_{OC}. The symmetry is also the origin of the 0.6% (absolute) higher fill factor predicted by the model. Obviously, a stronger asymmetry between electron and hole parameters will produce larger differences, which is one of the reasons the present model is not suited for a-Si solar cells.

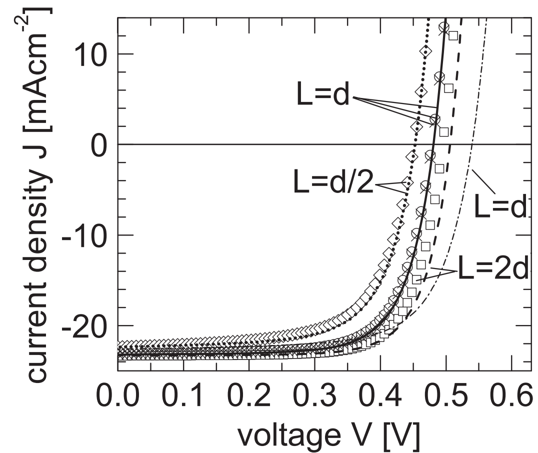

Figure 3. Illuminated current (J)/voltage (V) curves for simulated (symbols) and analytically modeled (lines) *p-i-n* cells. The simulations consider lifetimes and mobilities that yield ambipolar diffusion lengths L of half/equal/twice the thickness d of the *i*-layer (diamonds, circles, squares). The modeled curves use a single value of the mobility and lifetime that matches the same ambipolar diffusion length from the simulations, where electron-hole mobilities differ by a factor 3. Despite considering unequal mobilities in the simulations and a nonuniform photogeneration rate, we notice a very good agreement between model and simulations. A better match for the case $L = d$ is obviously obtained when simulating with a unique carrier mobility and uniform photogeneration (crosses). The dash-dotted curve was obtained with the model for $L = d$ but assuming no potential drops at the *p-i* and *i-n* interfaces (mean field approximation).

UNCORRECTED PROOF

DOI: 10.1002/pip

Table I. Mobilities, lifetimes, ambipolar diffusion lengths, and generation rates for the simulations and analytical calculations of Figures 3 through 6.

Symbol or linetype	Mobilities μ_p/μ_n and μ (cm^2 Vs^{-1})	Lifetimes $\tau_n = \tau_p = \tau$ (ns)	Resulting ambipolar diffusion length L (μm)	Generation rate
Diamonds	7.5/25	34	1.0 (d/2)	depth-dependent
Circles	15/50	68	2.0 (d)	depth-dependent
Squares	30/100	136	4.0 ($2 \times d$)	depth-dependent
Dotted line	11.5	34	1.0 (d/2)	7.3×10^{20} cm^{-3} s^{-1}
Solid line, crosses, dash-dotted line	23	68	2.0 (d)	7.3×10^{20} cm^{-3} s^{-1}
Dashed line	46	136	4.0 ($2 \times d$)	7.3×10^{20} cm^{-3} s^{-1}

The effort put on the calculation of the field F_0 in the intrinsic layer becomes clear when comparing the dash-dotted line in Figure 3, which belongs to the mean field approximation (calculated by letting $V_0 \to V_{bi}$). The remaining parameters were set equal to the baseline case $(L = d)$. Evidently, neglecting the voltage drops at the *p-i* and *i-n* interfaces yields an error of 60 mV in the open-circuit voltage V_{OC}.

Figure 4 shows the dark $J(V)$ curves corresponding to the cases from Figure 3, where plots (a, b, c) belong to the diffusion lengths $L = d/2$, $L = d$, and $L = 2d$, respectively. The modeled curves (lines) match the simulations (symbols) in all three cases, with slight deviations. In plots (a) and (b), the modeled curves deviate from the simulations when approaching the highest voltage values of $V = V_0 = 0.58$ V, which is a consequence of entering the high-injection regime for which the model is not suited. The curve modeled by the mean field approximation (dash-dotted line in Figure 4(b)) deviates considerably from the simulations already above a voltage of only 0.2 V, reaching almost an order of magnitude deviation from the simulations at the maximum voltage value. Finally, we mention that taking equal mobility values did not affect the simulated dark $J(V)$ curves appreciably and was therefore not included in the figure.

The dark $J(V)$ curves are characterized in more depth by the ideality factor n_{id}, which was calculated at each voltage value by the equation

$$n_{id} = \left(V_t \frac{d \ln J(V)}{dV} \right)^{-1} \quad (25)$$

By evaluating numerically Eq. (25) for the curves in Figure 4, we obtain the voltage-dependent ideality curves shown in Figure 5, where it is seen that when $V >> V_t$, the ideality factor lies in the range $1 \leq n_{id} \leq 2$. Although the first boundary condition from Eq. (13) is the main source for an ideality $n_{id} = 2$, the remaining voltage-dependent factors in J_{dark} (Eq. (18)) are responsible for $1 \leq n_{id} \leq 2$ and for the

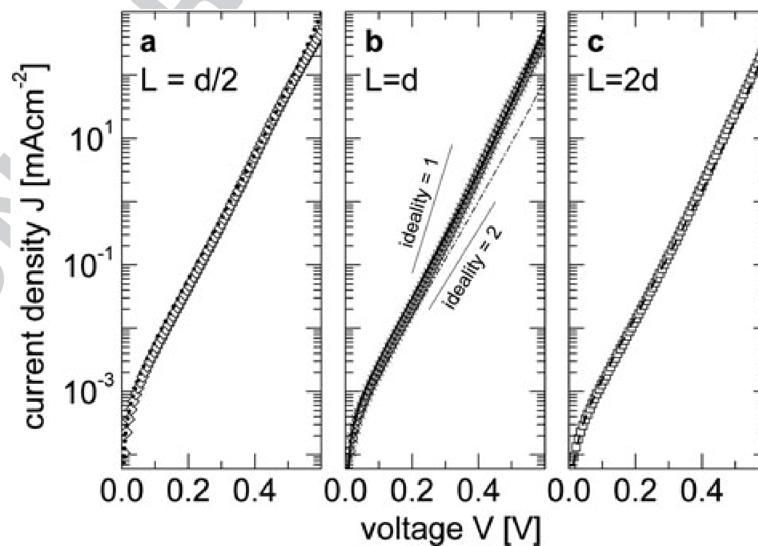

Figure 4. Dark current (J)/voltage (V) curves for simulated (symbols) and analytically modeled (lines) *p-i-n* cells having the same electronic parameters as in Figure 3. The simulations consider lifetimes and mobilities that yield ambipolar diffusion lengths L of half/equal/twice the thickness d of the i-layer (diamonds, circles, squares). The modeled curves use a single value of the mobility and lifetime that matches the same ambipolar diffusion length from the simulations.

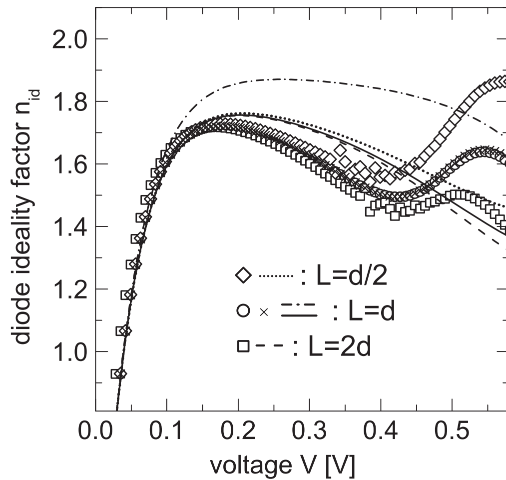

Figure 5. Voltage-dependent ideality factor n_{id} extracted from the dark *J*(*V*) curves for simulated (symbols) and modeled (lines) curves. In the voltage range relevant under solar operation (up to 0.5 V), the simulated ideality stays between 1.45 and 1.75, showing a local maximum at about 0.15 V. The model also shows a local maximum followed by a decrease towards higher voltages. Above 0.5 V, the solar cell enters high-injection conditions. The dash-dotted curve shows the ideality that would produce the model under the mean field approximation.

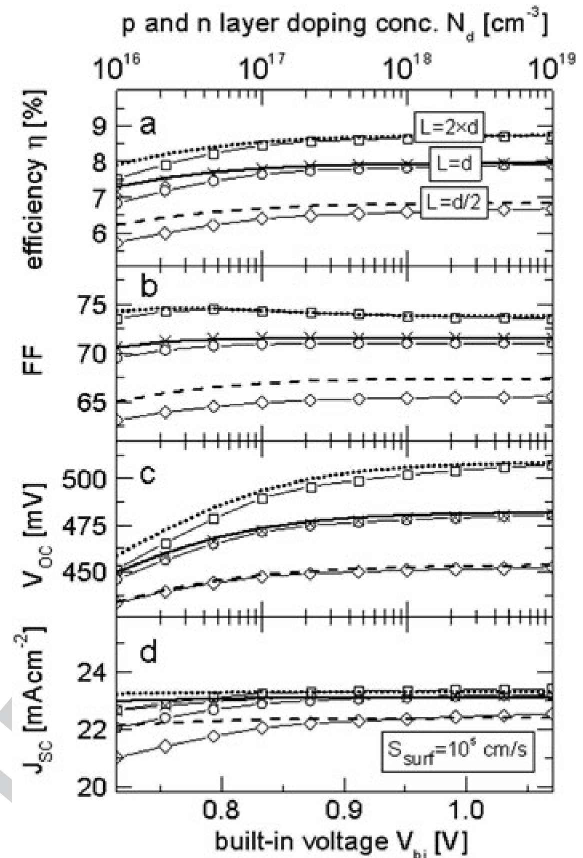

Figure 6. Simulated (symbols) and modeled (lines) homojunction *p-i-n* solar cell efficiency η, fill factor *FF*, open-circuit voltage V_{OC}, and short-circuit current density J_{SC} as a function of the built-in voltage V_{bi} (bottom axis) or, equivalently, *p*-layer and n-layer doping concentration N_d (top axis). Overall, the model follows the simulations for all three cases: diffusion length double ($L = 2 \times d$), equal ($L = d$), and half ($L = d/2$) the *i*-layer thickness. The main deviations between model and simulations arise at low built-in voltages, being 8% the highest relative error in η seen at $N_d = 10^{16}\,cm^{-3}$ ($V_{bi} = 0.71$ V). The lines connecting the simulation points are a guide to the eye.

voltage-dependent ideality. In standard *p-n* junction theory, $n_{id} = 2$ is identified as a fingerprint value for junction recombination, whereas $n_{id} = 1$ is attributed to neutral region recombination. Idealities deviating from these values may be a consequence of more complex recombination mechanisms or simply originate in the spatial distribution of minority carriers. Because in the present case, only one recombination mechanism is present, it is the spatial distribution of carriers that originates the observed voltage-dependent n_{id}.

As seen in Figure 5, the model reproduces well the initial increase of n_{id}, the local maximum, and the further decrease of n_{id} with voltage up to about $V = 0.4$ V. For higher bias values, the n_{id} values from the simulations increase again up to a new maximum value. Note that the absence of this feature in the model may not be a serious limitation of the model because in practice, any solar cell exhibits an additional, larger external series resistance that may dominate this part of the *J*(*V*) curve. Figure 5 also shows that the mean field approximation (dash-dotted line compared with circles and crosses) would yield an overall much higher n_{id} than the ideality from the simulations.

Let us now evaluate the incidence of the interface potential drops by varying the doping of the *n*-layer and *p*-layer, and hence the potentials V_{bi} and V_0. Figure 6 compares the efficiency η, fill factor *FF*, open-circuit voltage V_{OC}, and short-circuit current density J_{SC} of simulated (symbols) and modeled (lines) solar cells as a function of the doping N_d of the *n*-layer and *p*-layer (top horizontal axis). The chosen doping range $10^{16}\,cm^{-3} \leq N_d \leq 10^{19}\,cm^{-3}$ results in built-in voltages that span from $V_{bi} = 0.71$ V to $V_{bi} = 1.07$ V, as read from the bottom horizontal axis. The surface recombination velocity was set to $S_{surf} = 10^5\,cm\,s^{-1}$, and the mobilities and lifetimes were chosen according to the values shown in Table I to yield the three cases $L = d/2$ (diamonds, dotted line), $L = d$ (circles, crosses, solid line), or $L = 2d$ (squares, dashed line). The modeled open-circuit voltage V_{OC} (plot c) follows the simulations correctly in all three diffusion length cases, whereas the modeled short circuit current density J_{SC} (plot d) tends to be increasingly overestimated with decreasing built-in potential, although the deviation in J_{SC} stays below 5.2% relative. Overall, the maximum deviation is found for the case $L = d/2$ at $N_d = 10^{16}\,cm^{-3}$, with an 8.1/2.5/0.2/5.2% relative error in η, V_{OC}, *FF*, and J_{SC}, respectively. Above $N_d = 10^{17}\,cm^{-3}$, the analytical model follows accurately the simulations, with an overall maximum

error of 5% relative in η at $N_d = 10^{17}\ \mathrm{cm}^{-3}$ and $L = d/2$. This error decreases with increasing doping or L/d ratio. The main deviations between model and simulations arise from the asymmetry in carrier parameters and from the nonhomogeneous generation rate. Indeed, a closer match is seen in Figure 6 between the simulations of the symmetrical case and $L = d$ (crosses) and the modeled case (solid line). Specially, the stronger incidence of symmetry is seen in J_{SC}, where the deviation between model and simulation is reduced to half the deviation of the asymmetric case. Remaining differences must be found in the linearization of the recombination rate and the constant field approximation.

In Figure 7, we compare the simulated (symbols) and modeled (lines) efficiency η as a function of the built-in voltage at different surface recombination velocities S_{surf}, taking the case $L = d$. The remaining simulation and modeling parameters are identical to the baseline case described earlier. Overall, we see a good match between modeled and simulated curves, although the model tends to overestimate the efficiency. When analyzing the corresponding J_{SC}, FF, and V_{OC} results (not shown in Figure 7), it becomes evident that the higher modeled η arises again from J_{SC}, revealing a relative insensitivity of J_{SC} to S_{surf} within the model. This originates mainly in the assumption of the homogeneous generation rate, which tends to underestimate the higher number of electron-hole pairs generated near the front surface that may recombine there and are thus prevented from being collected. Nevertheless, the results from Figure 7 show a maximum deviation in η of nearly 7% (relative) at $V_{bi} = 0.71$ V and $S_{surf} = 10^6\ \mathrm{cm\,s}^{-1}$. In cells having larger built-in voltages

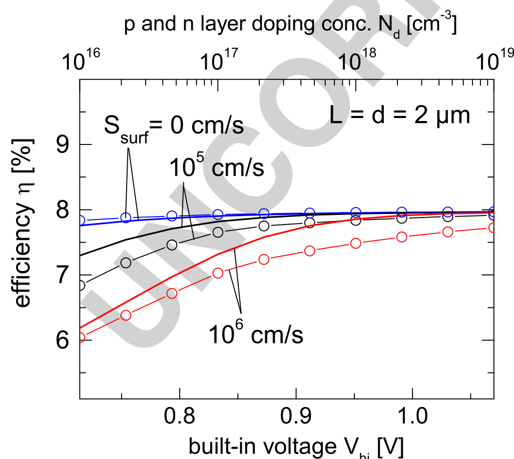

Figure 7. Efficiency η as a function of built-in voltage V_{bi} of cells simulated (symbols) and modeled (solid lines) with surface recombination velocities $S_{surf} = 0$, 10^5 and $10^6\ \mathrm{cm\,s}^{-1}$, in a *p-i-n* cell where the ambipolar diffusion length equals the *i*-layer thickness. The model follows the overall trend of η with V_{bi} and S_{surf} with a maximum overestimation of η of 7% (relative) at the lowest V_{bi} and $S_{surf} = 10^5\ \mathrm{cm\,s}^{-1}$. The lines connecting the simulation points are a guide to the eye.

or more homogeneous generation, the model will show a smaller deviation in J_{SC} and thus of η.

In conclusion, the comparisons between the numerical experiments and the theoretical curves reveal that over practical ranges of the most important physical quantities arising in a typical μc-Si (or similar) *p-i-n* cell, the present model is an accurate simplification for the case of a *p-i-n* solar cell with high light trapping and defect controlled recombination characterized by an injection-independent carrier lifetime. In the next section, we apply the model to fit experimental *p-i-n* solar cell data.

4. COMPARISON TO EXPERIMENTS

The model is now tested on $J(V)$ characteristics of state-of-the-art solar cells made from thin-film silicon material. This material is chosen because it is amongst the most relevant in photovoltaics based on *p-i-n* junctions. Additionally, mature nc-Si and μc-Si material is well known and characterized, making a comparison between fitted parameters and typical literature values straightforward.

First, we study a 9% efficient *p-i-n* solar cell that uses a 3.1 μm thick nc-Si *i*-layer with a crystallinity around 50%, which was prepared by a VHF glow discharge method [24]. The corresponding experimental $J(V)$ curves were provided by United Solar Ovonic LLC [25], shown in Figure 8 by square data points. The cell uses heterojunction interfaces of very thin a-Si *p* and *n* layers, which also serve to reduce surface recombination and shunt losses [26,27]. The layer stack is completed by a highly reflective ZnO/Ag back surface reflector and electrical contact, and a textured ITO front contact [28]. Further details about the fabrication of the device can be found in References [27,29].

By inspecting the dark $J(V)$ curve of Figure 8(b) (squares), we notice that this cell has a negligible shunt resistance effect, which is precisely the achievement of the optimization of the thickness of the doped a-Si layers [26]. Indeed, the inverse slope of the dark $J(V)$ curve at $V = 0$ yields a shunt resistance $r_{shunt} = 150\ \mathrm{k\Omega cm^2}$ [30]. Given this very high value, in the following, we neglect the effect of the shunt resistance, including only the series resistance effect by subtracting the voltage drop across the series resistance to the applied voltage. The fitting procedure consists therefore in finding the global minimum of the error function $f_{error} = J_{exp} - J(V_{exp} - J_{exp} \times r_s)$, where V_{exp} and J_{exp} are the experimental values, r_s is the specific series resistance, and J is evaluated from Eq. (15) through (18). The minimization procedure uses a simulated annealing algorithm with a tolerance of 10^{-6}. The excellent fit to the illuminated curve shown by the solid line in Figure 8(a) was obtained using five parameters: recombination lifetime $\tau = 250$ ns, mobility $\mu = 17.3\ \mathrm{cm^2\,V s^{-1}}$, effective recombination velocity $S = 1.5 \times 10^2\ \mathrm{cm\,s^{-1}}$, built-in voltage $V_{bi} = 872$ mV, and specific series resistance $r_s = 1.67\ \Omega\mathrm{cm}^2$. The value of the generation rate $G = 5.4 \times 10^{20}\ \mathrm{cm}^{-3}$ was adjusted to match the short-circuit current density of 26.4 mAcm^{-2}. Such a value for a mean generation rate seems reasonable for this 3.1 μm thick *i*-layer

UNCORRECTED PROOF

DOI: 10.1002/pip

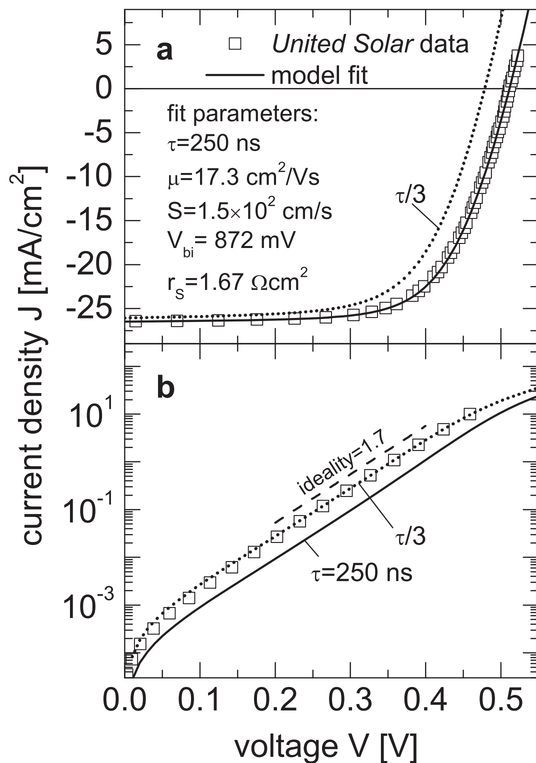

Figure 8. Measured (symbols) and modeled (lines) current density (J)/voltage (V) curves of heterojunction *p-i-n* solar cells based on nanocrystalline silicon. Plot (a) shows the illuminated J (V) curve, which the model accurately fits (solid line) using five parameters: minority carrier lifetime τ, mobility μ, effective recombination velocity S, built-in voltage V_{bi}, and specific series resistance r_s. The dashed line in plot (a) uses a lifetime divided by 3. When the dark $J(V)$ curve seen in plot (b) is modeled using the same parameters as the light $J(V)$ fit, the modeled curve (solid line) shows the same diode ideality of 1.7 but appears shifted downwards in J. An excellent fit to the dark curve is recovered when dividing the lifetime by 3 and keeping the remaining parameters.

with high light trapping [28]. The remaining parameters utilized in the fit are standard crystalline silicon values at 298 K temperature: intrinsic carrier concentration $n_i = 3.45 \times 10^{10}\,\mathrm{cm}^{-3}$ and relative dielectric constant $\varepsilon = 11.9$ [2].

Now, we proceed to analyze in some detail the obtained parameter values. First, let us estimate the effect of the voltage drop at the interfaces occurring in the cell under study. With n_i and ε, we obtain a Debye–Hückel length in the intrinsic layer of $L_i = 36.6\,\mu\mathrm{m}$ and a thickness to L_i ratio of $d/L_i = 0.085$. If we use this value to enter in Figure 2 with $V_{bi}/V_t = 0.872\,\mathrm{V}/0.025\,\mathrm{V} \approx 35$ ($V_0 = 0.54\,\mathrm{V}$), we read on the vertical axis that the field F_0 in the *i*-layer is roughly 70% the value of the mean field given by V_{bi}/d. Second, regarding the obtained mobility and lifetime, note that if we calculate the mobility-lifetime product, we obtain $\mu\tau = 4.3 \times 10^{-6}\,\mathrm{cm}^2\,\mathrm{V}^{-1}$, which is on the upper range of the values reported in nc-Si literature [31]. This value corresponds to a diffusion length of $L = 3.3\,\mu\mathrm{m}$, comparable with the 3.1 μm thick *i*-layer. Last, let us analyze the seemingly low effective recombination velocity. In Eq. (23), with an nc-Si/a-Si conduction band offset of $\Delta E_C = 0.1\,\mathrm{eV}$ [32,33], taking the aforementioned V_{bi} and V_0 values, we obtain $S_{int} + S_{surf} = 5.4 \times 10^6\,\mathrm{cm\,s}^{-1}$. Although this is a maximum estimate because recombination losses at *n*-layer were neglected, we notice that this value corresponds to unpassivated semiconductor-contact surfaces.

Now, we proceed to the dark $J(V)$ curves shown in Figure 8(b) (squares: data, lines: model). When the fit parameters from the illuminated $J(V)$ curve are introduced into the dark current/voltage characteristics, we obtain the solid line in Figure 8(b), which shows practically the same logarithmic slope as the data, corresponding to an ideality of 1.7. However, the computed curve appears displaced downwards in the logarithmic scale, seemingly pointing to a lower required lifetime value. Indeed, when using a lifetime of 250/3 ns = 83.3 ns with the remaining parameters left unchanged, we obtain the fit shown by dotted lines in Figure 8(b). A possible source for the need of a lower lifetime under dark—as opposed to illumination conditions—could be defect recombination at the a-Si/μc-Si interfaces, as observed in crystalline–amorphous Si solar cells [34]. Another possible source is the light-controlled charging state of defects such as in aluminum-doped Czochralski silicon, where deep defects result in increasing lifetimes when going from very low illumination to typical solar illumination conditions [35] or in cases where different recombination mechanism dominate at low/moderate injection [36]. For the nc-Si solar cell under study, more experimental research is needed to resolve the apparent increase of lifetime with illumination.

An important final remark on the illuminated curve of Figure 8(a) must be made regarding the voltage-dependent photocurrent. Notice that a direct calculation of the experimental photocurrent as the difference between light and dark currents is not desirable here because from the previous analysis, this cell apparently has an illumination-dependent lifetime, meaning that the dark component of the illuminated $J(V)$ curve is not available. However, we can indirectly check the behavior of the voltage-dependent photocurrent by evaluating the model at low bias voltages, where the photocurrent dominates. Because at low bias the current of the studied cell varies only slowly with voltage, the differential resistance dV/dJ is a more adequate quantity to reflect the voltage-dependent photocurrent. Figure 9 therefore shows dV/dJ as a function of voltage, revealing that the model (solid line) correctly follows the experimental data also at low bias voltages. Notice that under the one-diode model of a solar cell, the value of dV/dJ at $V = 0$ would be interpreted as a shunt resistance, which in this case would be $r_{shunt} = dV/dJ$ 1.5 kΩcm² [30], that is two orders of magnitude lower than the value from the dark $J(V)$ analysis mentioned earlier. Furthermore, when fitting the illuminated $J(V)$ curve with a one-diode model fixing $r_{shunt} = 1.5\,\mathrm{k\Omega cm}^2$, $r_s = 1.67\,\Omega\mathrm{cm}^2$ (as determined previously) and a constant photocurrent equal to the short-circuit value [30], we obtain an ideality of 1.59 and a saturation current density of $7.9 \times 10^{-8}\,\mathrm{Acm}^{-2}$, which

UNCORRECTED PROOF

Prog. Photovolt: Res. Appl. (2012) © 2012 John Wiley & Sons, Ltd.
DOI: 10.1002/pip

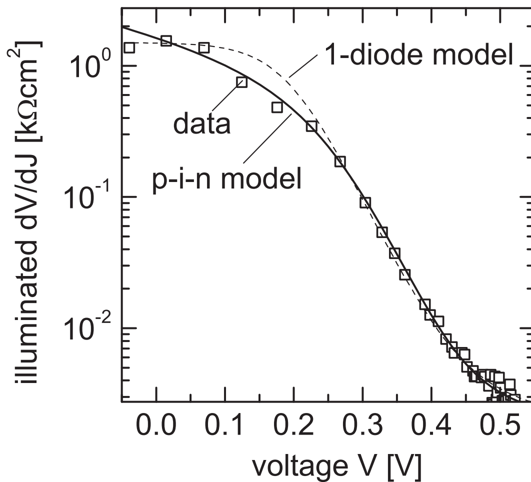

Figure 9. Differential specific resistance *dV/dJ* calculated from the illuminated *J*(*V*) curves shown in Figure 8(a). This plot highlights the dependence of the illuminated current as a function of voltage for low bias voltages, showing that the *p-i-n* model (solid line) follows the data (square symbols). For comparison, the dashed line is the result of fitting the illuminated *J*(*V*) curve with a one-diode model where the shunt resistance is fixed by the slope of the *J*(*V*) data at short-circuit conditions.

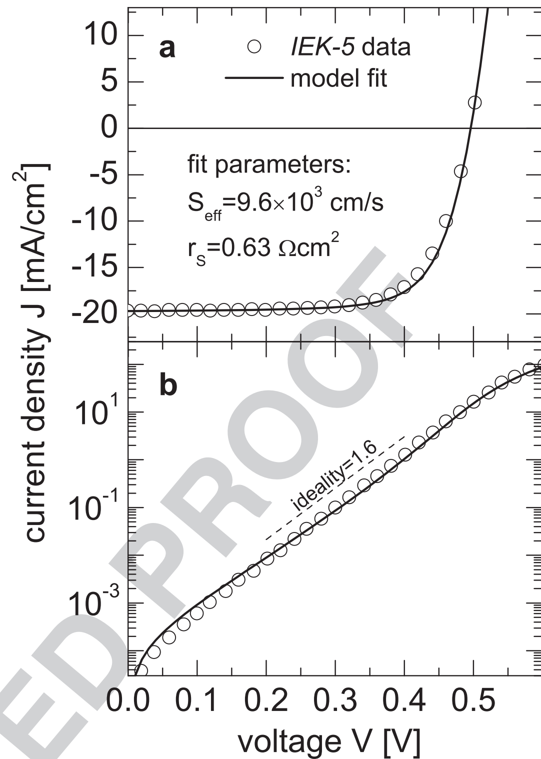

Figure 10. Measured (symbols) and modeled (lines) current density (*J*)/voltage (*V*) curves of microcrystalline silicon *p-i-n* solar cells. Plot (a) shows the illuminated *J*(*V*) curve fitted by the model using only two parameters: effective surface recombination velocity *S* and specific series resistance r_s. The remaining parameters are known from a previous study [37]. In plot (b), the measured dark curve is modeled with the same parameters as the light *J*(*V*) fit, yielding an overall diode ideality of 1.6.

yield a nearly identical *J*(*V*) curve as the solid line in Figure 8 (a) (excluded from the plot for clarity). However, when evaluating the corresponding *dV*/*dJ* curve corresponding to the one-diode model fit, we obtain the dashed line in Figure 9, which remains nearly constant at low bias voltages, as opposed to the variation seen in the data or the *p-i-n* model. This supports the argument that the slope of the illuminated *J*(*V*) curve originates in the voltage dependence of the photocurrent and not in shunt effects.

The next studied case is a 6.9% efficient μc-Si *p-i-n* solar cell optimized for triple-junction a-Si/μc-Si cells, prepared at the IEK-5 laboratories [37]. It consists of a 1.15 μm thick *i*-layer of 60% crystalline volume fraction, which is placed between a μc-Si *p*-type front layer and an a-Si *n*-layer that also reduces back surface recombination. The measured light and dark current/voltage characteristics from Reference [37] are shown by the circles data in **F10** Figure 10(a) and (b), respectively. From the dark *J*(*V*) curve, we notice that also in this case, there are no significant shunt effects.

In this device, several parameters are known a priori from the characterization of individual layers and detailed device analyses reported by Pieters *et al.*[37]. For instance, the activation energies of the doped layers reported in References [37,38] result in a built-in voltage $V_{bi} = 810\,\mathrm{mV}$, whereas the carrier mobilities determined experimentally on the same material [39,38] are $\mu_n = 50\,\mathrm{cm^2\,Vs^{-1}}$ and $\mu_p = 15\,\mathrm{cm^2\,Vs^{-1}}$, implying that the value of the ambipolar mobility needed by our model is $\mu = 23\,\mathrm{cm^2\,Vs^{-1}}$. Furthermore, the recombination parameters in the cell were extracted by numerical simulation of the complete device considering recombination at dangling bonds, bandtails and front/back interface defects [37]. Simultaneous fits with the numerical model to four characteristic curves, namely light and dark current/voltage curves, voltage-dependent activation energy curve, and quantum efficiency spectrum resulted in the SRH minority carrier lifetime (equal for both carrier types) of $\tau_{0,n/p} = 66.7\,\mathrm{ns}$, bandtail capture rates at neutral defect states of $5 \times 10^9\,\mathrm{cm^3\,s^{-1}}$, and infinite front/back surface recombination velocities [37]. Because in Reference [37] bandtail recombination was shown to compete with dangling bond recombination for voltages above the open-circuit voltage, the model was evaluated using only the SRH lifetime, that is using $\tau = 66.7\,\mathrm{ns}$. The front/back contact recombination was incorporated as the effective recombination velocity *S*, which is a fit parameter together with the specific series resistance r_s. Therefore, we are left with only two fit parameters, a much more restrictive situation than in the previous analysis of the nc-Si cell.

The solid line in Figure 10(a) shows the fit to the illuminated *J*(*V*) curve, using an effective recombination velocity $S = 9.56 \times 10^3\,\mathrm{cm\,s^{-1}}$ and a specific series resistance $r_s = 0.63\,\Omega\mathrm{cm}^2$. Again, the value of the generation rate

UNCORRECTED PROOF

$G = 1.08 \times 10^{21}\ \mathrm{cm}^{-3}$ was adjusted to match the short-circuit current density. The built-in voltage and thickness in this cell establish that the equilibrium *i*-layer potential is $V_0 = 647\ \mathrm{mV}$. Despite its lower built-in voltage, V_0 is larger than in the previous nc-Si cell because of the nearly three-fold lower thickness. We can now use V_0 to predict the effective recombination velocity, similarly to the previous case. In Eq. (21), we obtain $S_{int} + S_{surf} = 2.18 \times 10^5\ \mathrm{cm\,s}^{-1}$.

When plotting the dark $J(V)$ curve using the same parameters as the illuminated curve, we obtain the solid line of Figure 10(b), also resulting in a good fit to the data. Figure 11 shows the voltage-dependent ideality that results from computing Eq. (25) on the data (circles data) and the model fit (solid line). The ideality oscillates between 1.0 and 1.88 up to 0.52 V, where the effect of the series resistance sets in. Despite the noise in the data, we see that the fit tends to slightly overestimate n_{id} below 0.3 V, which is also seen by the smaller slope of the $J(V)$ curve in Figure 10 (b). Above 0.3 V, the model fits the data more accurately, showing a minimum of $n_{id} = 1.36$ at 0.42 V. An appropriate task for future investigations could be the investigation of the ideality interpreted from V_{OC} versus $\ln(J_{SC})$ curves from light-dependent $J(V)$ measurements.

As a final note, we may let the model forecast a few efficiency improvements. For example, if we divide the actual series resistance $r_s = 0.63\ \Omega\mathrm{cm}^2$ by a factor 2, the calculated efficiency increases from $\eta = 7.04\%$ to $\eta = 7.14\%$, whereas a reduction in r_s by a factor 10 would yield $\eta = 7.22\%$. Any of these cases leads to higher improvements than increasing V_{bi} from 810 mV by nearly 10% to the value $V_{bi} = 890\ \mathrm{mV}$, which yields $\eta = 7.11\%$. Obviously, more significant improvements are obtained by reducing recombination. A factor 10 reduction in S_{eff} enables an efficiency of $\eta = 7.50\%$, whereas a factor 2 increase in τ, that is a reduction of 50% in terms of overall defect concentration, would yield $\eta = 7.30\%$.

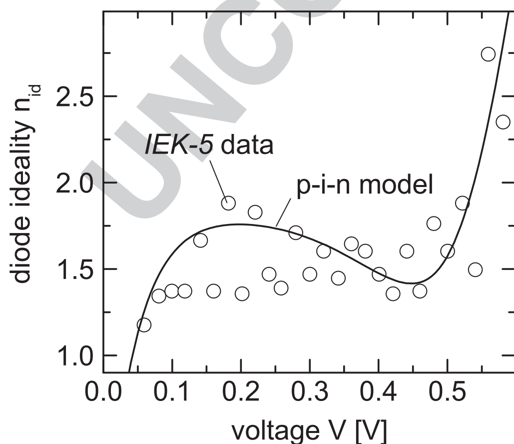

Figure 11. Diode ideality as a function of voltage for the μc-Si *p-i-n* solar cell, as calculated from the dark current/voltage curves from Figure 10(b) using Eq. (25). The circles belong to the measured data and the solid line to the fit.

5. CONCLUSIONS

A detailed analysis of the electric field in *p-i-n* solar cells allows obtaining simple analytical estimates for the potential drops at the *p-i* and *i-n* interfaces. For typical *p-i-n* solar cells, it is shown that the resulting potential difference in the *i*-layer is considerably smaller than the built-in voltage. This leads to accurate analytical estimates for both the electric field in the *i*-layer and for the surface/interface recombination velocities expressed as an effective recombination velocity at the limits of the *i*-layer.

The new estimate for the electric field is introduced in an analytical model for the current (J)/voltage (V) characteristics of *p-i-n* solar cells under low-injection conditions, assuming drift and diffusion currents. Interestingly, no additional device or material parameters are required than in the classical mean-field approximation. The resulting closed-form expression of the $J(V)$ curve is validated by numerical device simulations, showing that the new estimate for the electric field at the *i*-layer is crucial to model *p-i-n* solar cells with realistic parameters.

By including the effect of series resistance, the model is able to successfully fit experimental $J(V)$ curves of state-of-the-art *p-i-n* nc-Si and μc-Si solar cells. The fits reproduce light and dark $J(V)$ curves, including the values of the ideality factors in the dark (around 1.6–1.7), and the nonnegligible slopes of the photocurrent near zero voltage, which are correctly explained by the voltage-dependent photocurrent of the model. The fit parameters agree with values of optimized solar cells commonly reported in the literature.

ACKNOWLEDGEMENTS

The author acknowledges B. Yan and J. Yang from United Solar Ovonic LLC [25] for kindly providing the solar cell data and sharing his views on the model, U. Rau and B. Pieters from IEK-5 [40], and M. Soldera for thoroughly revising the manuscript and testing the equations. This work was supported by CONICET and Comahue National University (Argentina).

REFERENCES

1. Fonash SJ. *Solar Cell Device Physics*. Academic Press: Amsterdam, 2010; 73–83.
2. Sze SM, Ng KK. *Physics of Semiconductor Devices*, 3rd edn. Wiley-Interscience: Hoboken, 2006; 674.
3. Luque A, Hegedus S. *Handbook of Photovoltaic Science and Engineering*. John Wiley & Sons: Chichester, 2010; 125.
4. Brabec C, Scherf U, Dyakonov V. *Organic Photovoltaics: Materials, Device Physics, and Manufacturing Technologies*, 1st edn. Wiley-VCH: Weinheim, 2008; 286.
5. Lang JR, Neufeld CJ, Hurni CA, Cruz SC, Matioli E, Mishra UK, Speck JS. High external quantum efficiency

UNCORRECTED PROOF

and fill-factor InGaN/GaN heterojunction solar cells grown by NH3-based molecular beam epitaxy. *Applied Physics Letters* 2011; **98**: 1311151–1311153.
6. Rau U, Abou-Ras D, Kirchartz T. *Advanced Characterization Techniques for Thin Film Solar Cells*. John Wiley & Sons: Weinheim, 2011; 529.
7. Snowden CM. *Introduction to Semiconductor Device Modelling*. World Scientific: Singapore, 1987; 1.
8. Selberherr S. *Analysis and simulation of semiconductor devices*. Springer Science & Business: Vienna, 1984; 1.
9. Schiff EA. Low-mobility solar cells: a device physics primer with application to amorphous silicon. *Solar Energy Materials and Solar Cells* 2003; **78**: 567–595.
10. Liou JJ. *Advanced Semiconductor Device Physics and Modeling*. Artech House: London, 1994; 407.
11. Irrera F, Palma F. Toward an analytical solution of the hydrogenated amorphous silicon p-i-n structure: Hyperbolic approximation of nonuniform electric field. *Journal of Applied Physics* 1989; **66**: 3661–3665.
12. Crandall RS. Modeling of thin film solar cells: Uniform field approximation. *Journal of Applied Physics* 1983; **54**: 7176–7186.
13. Pezzimenti F, Albanese LF, Bellone S, Corte F. Analytical model for the forward current of Al implanted 4 H-SiC p-i-n diodes in a wide range of temperatures. *Bipolar/BiCMOS Circuits and Technology Meeting, 2009. IEEE* 2009, pp. 214 –217.
14. Crandall RS. Transport in hydrogenated amorphous silicon p-i-n solar cells. *Journal of Applied Physics* 1982; **53**: 3350–3352.
15. Merten J, Asensi JM, Voz C, Shah AV, Platz R, Andreu J. Improved equivalent circuit and analytical model for amorphous silicon solar cells and modules. *IEEE Transactions on Electron Devices* 1998; **45**: 423–429.
16. Brammer T, Stiebig H. Applying analytical and numerical methods for the analysis of microcrystalline silicon solar cells. *Solar Energy Materials and Solar Cells* 2006; **90**: 3021–3030.
17. Taretto K, Rau U, Werner JH. Closed-form expression for the current/ voltage characteristics of p-i-n solar cells. *Applied Physics A: Materials Science and Processing* 2003; **77**: 865–871.
18. Gemmer C. Analytische und numerische Untersuchungen von Solarzellen unter wechselnden Beleuchtungsbedingungen. PhD Thesis, Stuttgart University, Stuttgart, Germany, 2003; 66.
19. Al Tarabsheh A. Amorphous Silicon Based Solar Cells. PhD Thesis, Stuttgart University, Stuttgart, Germany, 2007; 33.
20. Davis H. *Introduction to nonlinear differential and integral equations*. Dover Publications: New York, 1962; 192.
21. Smith P, Jordan D, Jordan DW. *Nonlinear Ordinary Differential Equations: An Introduction for Scientists and Engineers*, 4th edn. Oxford University Press: Oxford, 2007; 159.
22. Byrd PF, Friedman MD. *Handbook of elliptic integrals for engineers and scientists*, 2nd edn. Springer: New York, 1971; 29.
23. Nelson J. *The Physics of Solar Cells*. Imperial College Press: London, 2003; 191.
24. Yan B. personal communication, 24-May-2012.
25. United Solar Ovonic LLC. Troy (Michigan), U.S.A. 2012. http://www.uni-solar.com.
26. Yue G, Yan B, Teplin C, Yang J, Guha S. Optimization and characterization of i/p buffer layer in hydrogenated nanocrystalline silicon solar cells. *Journal of Non-Crystalline Solids* 2008; **354**: 2440–2444.
27. Yan B, Yang J, Guha S. Amorphous and nanocrystalline silicon thin film photovoltaic technology on flexible substrates. *Journal of Vacuum Science Technology A: Vacuum, Surfaces, and Films* 2012; **30**: 04D108–04D108–10.
28. Yue G, Sivec L, Owens JM, Yan B, Yang J, Guha S. Optimization of back reflector for high efficiency hydrogenated nanocrystalline silicon solar cells. *Applied Physics Letters* 2009; **95**: 263501–263501–3.
29. Yang J, Guha S. Status and future perspective of a-Si:H, a-SiGe:H, and nc-Si:H thin film photovoltaic technology. *Proceedings of SPIE* 2009; **7409**: 74090C–74090C–14.
30. Ishibashi K, Kimura Y, Niwano M. An extensively valid and stable method for derivation of all parameters of a solar cell from a single current-voltage characteristic. *Journal of Applied Physics* 2008; **103**: 094507–094507.
31. Poortmans J, Arkhipov V. *Thin film solar cells: fabrication, characterization and applications*. John Wiley & Sons: Hoboken, 2006; 148.
32. Essick JM, Nobel Z, Li Y-M, Bennett MS. Conduction- and valence-band offsets at the hydrogenated amorphous silicon-carbon/crystalline silicon interface via capacitance techniques. *Physical Review B* 1996; **54**: 4885–4890.
33. Mimura H, Hatanaka Y. Energy–band discontinuities in a heterojunction of amorphous hydrogenated Si and crystalline Si measured by internal photoemission. *Applied Physics Letters* 1987; **50**: 326–328.
34. Garín M, Rau U, Brendle W, Martín I, Alcubilla R. Characterization of a-Si:H/c-Si interfaces by effective-lifetime measurements. *Journal of Applied Physics* 2005; **98**: 093711–093711–9.
35. .Schmidt J. Temperature- and injection-dependent lifetime spectroscopy for the characterization of defect centers in semiconductors. *Applied Physics Letters* 2003; **82**: 2178–2180.

UNCORRECTED PROOF

36. Kerr LL, Li SS, Johnston SW, Anderson TJ, Crisalle OD, Kim WK, Abushama J, Noufi RN. Investigation of defect properties in $Cu(In,Ga)Se_2$ solar cells by deep-level transient spectroscopy. *Solid State Electronics* 2004; **48**: 1579–1586.
37. Pieters BE, Stiebig H, Zeman M, van Swaaij RACMM. Determination of the mobility gap of intrinsic μc-Si:H in p-i-n solar cells. *Journal of Applied Physics* 2009; **105**: 044502-044502-10.
38. Pieters BE. Characterization of thin-film silicon materials and solar cells through numerical modeling. PhD Thesis, Delft University of Technology, Delft, Netherlands, 2008; 90.
39. Chan K-Y, Knipp D, Gordijn A, Stiebig H. Influence of crystalline volume fraction on the performance of high mobility microcrystalline silicon thin-film transistors. *Journal of Non-Crystalline Solids* 2008; **354**: 2505–2508.
40. IEK-5. Forschungszentrum Jülich, Germany. 2012. http://www.fz-juelich.de/iek/iek-5/EN/Home/home_node.html
41. Corless RM, Gonnet GH, Hare DEG, Jeffrey DJ, Knuth DE. On the LambertW function. *Advanced Computational Mathematics* 1996; **5**: 329–359.

APPENDIX A

Here, we obtain the approximation of the field F_0 in the center of the *i*-layer given by Eq. (5). The first term of the series expansion of the expression $-\mathrm{j} \times \mathrm{am}(-\mathrm{j} \times u, m)$ around $m=0$ is given by $-u+m(u/4-\sinh(2u)/8)$ plus second order terms. Because m tends to zero, the term $u/4$ in the parenthesis is neglected against $-u$. Thus, with $m=(2V_t/F_0L_i)^2$ and $u=F_0x/2V_t$, the first term of the series expansion of the electrostatic potential $\psi(x)$ in the *i*-layer given by Eq. (3) is approximated by

$$\psi(x) \cong -F_0x - \left(\frac{V_t}{F_0L_i}\right)^2 V_t \sinh(F_0x/V_t) \qquad \text{(A1)}$$

Computing the built-in voltage as $V_{bi}=\psi(d/2)-\psi(-d/2)$, we obtain the approximate expression

$$V_{bi} \cong F_0d + 2V_t\left(\frac{V_t}{F_0L_i}\right)^2 \sinh\left(\frac{F_0d}{2V_t}\right) \qquad \text{(A2)}$$

In practical solar cells, the argument of the "sinh" is much larger than 1, meaning that we can replace $\sinh(z)$ $\exp(z)/2$ without losing precision. Taking this into account enables to rearrange and solve for F_0 from Eq. (27) to obtain the following:

$$F_0 \cong -\frac{V_{bi}}{d} - \frac{2V_t}{d} W\left(\frac{1}{2}\left(\frac{V_t}{F_0L_i}\right)^2 \exp\left(\frac{V_{bi}}{2V_t}\right)\right) \qquad \text{(A3)}$$

where W is Lambert's W-function.[41] When the argument of $W(z)$ is larger than exp(1), we can take the first-order expansion of $W(z) \cong \ln(z)$. In Eq. (28), it is possible to show that this approximation holds for $d/L_i \geq \sqrt{2e}(V_{bi}/V_t)\exp(-V_{bi}/4V_t)$. Because, actually, $\ln(z)$ is somewhat larger than $W(z)$ when $z \geq e$, we compensate this by replacing F_0 by $-V_{bi}/d$ in the argument of $W(z)$. Taking this approximation into account and replacing $W(z) \rightarrow \ln(z)$ in Eq. (28), F_0 simplifies to

$$F_0 \cong -\frac{4V_t}{d} \ln\left(\frac{\sqrt{2}V_{bi}L_i}{V_td}\right) \qquad \text{(A4)}$$

Next, we show that the electrical field in the *i*-layer is nearly constant above a distance $\delta \cong 2V_t/F_0$ away from the *p-i* and *i-n* interfaces. Because the center of the *i*-layer is placed at $x=0$, and the factor multiplying the hyperbolic sine in Eq. (26) tends to zero, it holds that $\psi(x) \cong -F_0x$ over an interval around $x=0$ where the hyperbolic sine is negligible. Away from the *i*-layer center and approaching the *p-i* and *i-n* interfaces, however, the "sinh" term contributes significantly to the shape of $\psi(x)$. From Eq. (26), we can rewrite $\sinh(F_0x/V_t)=-\exp(-F_0x/V_t)/2+\exp(F_0x/V_t)/2$, which shows that after a distance V_t/F_0 away from the *p-i* and *i-n* interfaces, the contribution of the "sinh" term to $\psi(x)$ decays by the factor $\exp(-1)$, and after the distance $2V_t/F_0$, it decays by $\exp(-2)=0.13$. Thus, if we define $\delta \cong 2V_t/F_0$ (cf. Eq. (7) from the main text), we are accepting 13% error on the distance δ from the interfaces up to which the potential is nonlinear (nonconstant field).

APPENDIX B

The integration constants C_1 and C_2 for Eq. (11) are obtained by applying the boundary conditions given by Eqs (13) and (14), yielding

$$C_1 = n_0\left(-\frac{d}{2}\right)e^{\frac{\beta_1}{2}} \times \left(\upsilon - \gamma - \frac{e^{\frac{\varsigma_0}{2}}}{1-\varsigma_0\varsigma\Lambda^2} + A_3\right) \qquad \text{(B1)}$$

where $n_0\left(-\frac{d}{2}\right)$ is the equilibrium minority carrier concentration at $x=-d/2$ calculated from Eq. (10). The greek letters denote the dimensionless parameters $\varsigma=V/V_t$, $\varsigma_0=V_0/V_t$, $\upsilon=\exp\left(\frac{\varsigma+\varsigma_0}{2}\right)$, $\gamma=G\tau/n_0\left(-\frac{d}{2}\right)$, and $\Lambda=L/d$. The parameter A_3 is given by

$$A_3 = \frac{e^{-\frac{\beta_1}{2}}\left(\gamma(\varsigma-\varsigma_0-\sigma)+\frac{\varsigma\left(1+\Lambda^2\sigma\varsigma_0\right)}{1-\varsigma_0\varsigma\Lambda^2}\right)+(\sigma+\beta_2)\left(\gamma-\upsilon+\frac{e^{\frac{\varsigma_0}{2}}}{1-\varsigma_0\varsigma\Lambda^2}\right)}{\beta_2+\sigma+(\beta_1-\sigma)e^{-\frac{\beta_1+\beta_2}{2}}} \qquad \text{(B2)}$$

UNCORRECTED PROOF

Prog. Photovolt: Res. Appl. (2012) © 2012 John Wiley & Sons, Ltd.
DOI: 10.1002/pip

where $\sigma = SD/d$. The second integration constant C_2 is given by

$$C_2 = -n_0\left(-\frac{d}{2}\right)A_3 e^{-\frac{\beta_2}{2}} \quad \text{(B3)}$$

When calculating the current, these constants are expanded in order to rearrange the expression of $J(V)$ in terms of the dark current density and the photocurrent. Note that the expressions developed in this appendix are not required to compute the $J(V)$ equation from the main text.

UNCORRECTED PROOF

Author Query Form

Journal: Progress in Photovoltaics: Research and Applications

Article: pip_2325

Dear Author,

During the copyediting of your paper, the following queries arose. Please respond to these by annotating your proofs with the necessary changes/additions.

- If you intend to annotate your proof electronically, please refer to the E-annotation guidelines.
- If you intend to annotate your proof by means of hard-copy mark-up, please refer to the proof mark-up symbols guidelines. If manually writing corrections on your proof and returning it by fax, do not write too close to the edge of the paper. Please remember that illegible mark-ups may delay publication.

Whether you opt for hard-copy or electronic annotation of your proofs, we recommend that you provide additional clarification of answers to queries by entering your answers on the query sheet, in addition to the text mark-up.

Query No.	Query	Remark
Q1	AUTHOR: Please check the suitability of the suggested short title.	
Q2	AUTHOR: As per journal instruction, first name of authors should be spell out. Please check if this is correct.	
Q3	AUTHOR: Please provide a short 'GTOC' abstract (maximum 80 words or 3 sentences) summarizing the key findings presented in the paper for Table of Content (TOC) entry.	
Q4	AUTHOR Please define VHF.	
Q5	AUTHOR: Please define ITO.	

WILEY-BLACKWELL

USING e-ANNOTATION TOOLS FOR ELECTRONIC PROOF CORRECTION

Required software to e-Annotate PDFs: Adobe Acrobat Professional or Adobe Reader (version 7.0 or above). (Note that this document uses screenshots from Adobe Reader X)
The latest version of Acrobat Reader can be downloaded for free at: http://get.adobe.com/uk/reader/

Once you have Acrobat Reader open on your computer, click on the Comment tab at the right of the toolbar:

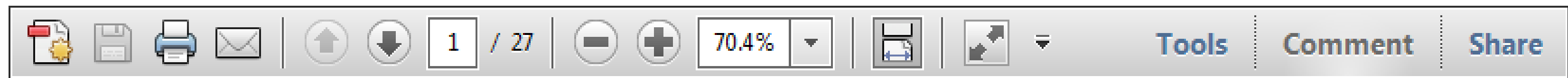

This will open up a panel down the right side of the document. The majority of tools you will use for annotating your proof will be in the Annotations section, pictured opposite. We've picked out some of these tools below:

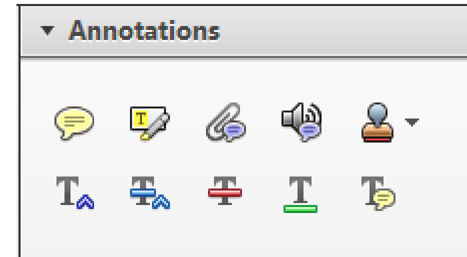

1. Replace (Ins) Tool – for replacing text.

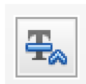

Strikes a line through text and opens up a text box where replacement text can be entered.

How to use it

- Highlight a word or sentence.
- Click on the Replace (Ins) icon in the Annotations section.
- Type the replacement text into the blue box that appears.

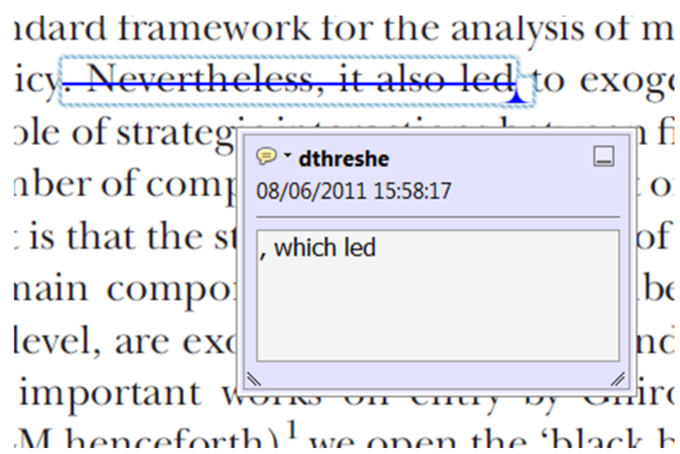

2. Strikethrough (Del) Tool – for deleting text.

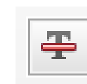

Strikes a red line through text that is to be deleted.

How to use it

- Highlight a word or sentence.
- Click on the Strikethrough (Del) icon in the Annotations section.

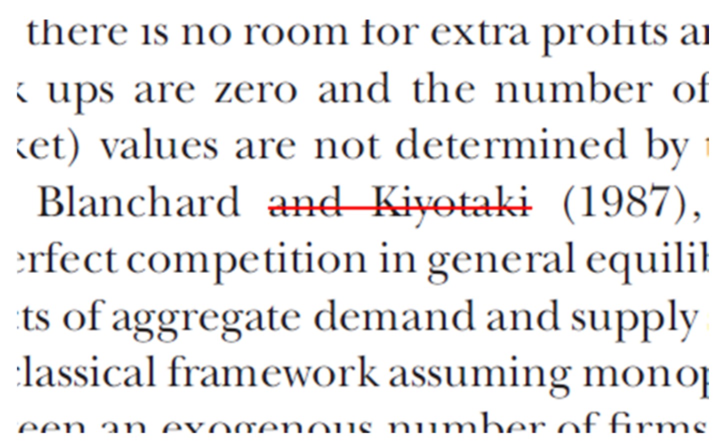

3. Add note to text Tool – for highlighting a section to be changed to bold or italic.

Highlights text in yellow and opens up a text box where comments can be entered.

How to use it

- Highlight the relevant section of text.
- Click on the Add note to text icon in the Annotations section.
- Type instruction on what should be changed regarding the text into the yellow box that appears.

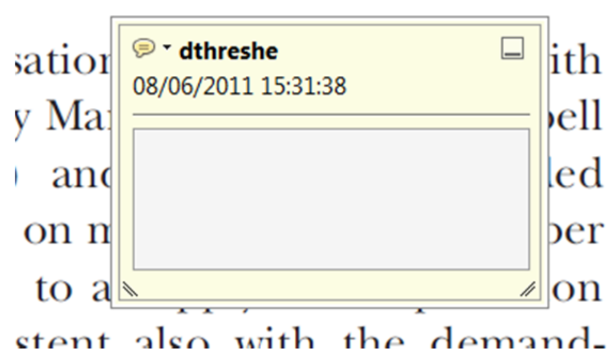

4. Add sticky note Tool – for making notes at specific points in the text.

Marks a point in the proof where a comment needs to be highlighted.

How to use it

- Click on the Add sticky note icon in the Annotations section.
- Click at the point in the proof where the comment should be inserted.
- Type the comment into the yellow box that appears.

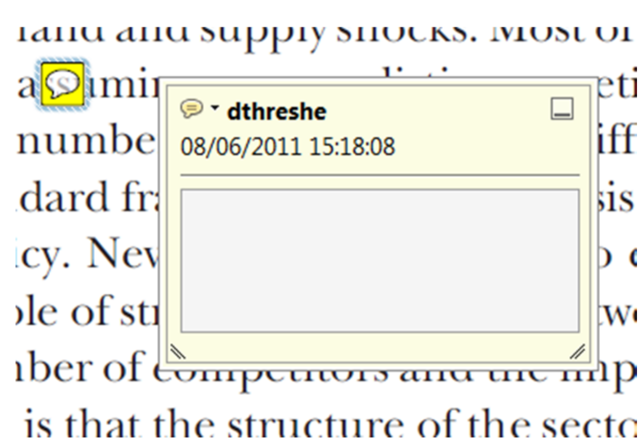

WILEY-BLACKWELL

USING e-ANNOTATION TOOLS FOR ELECTRONIC PROOF CORRECTION

5. Attach File Tool – for inserting large amounts of text or replacement figures.

Inserts an icon linking to the attached file in the appropriate pace in the text.

How to use it

- Click on the Attach File icon in the Annotations section.
- Click on the proof to where you'd like the attached file to be linked.
- Select the file to be attached from your computer or network.
- Select the colour and type of icon that will appear in the proof. Click OK.

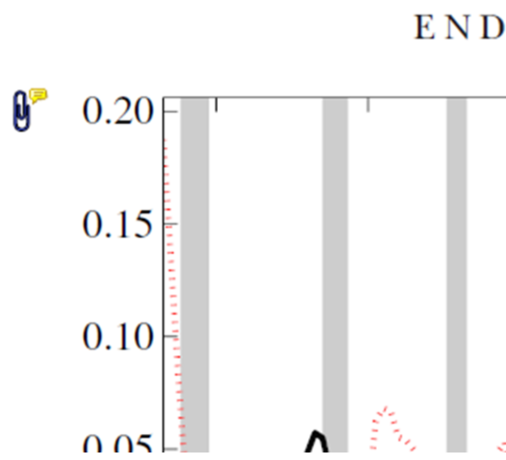

6. Add stamp Tool – for approving a proof if no corrections are required.

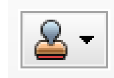

Inserts a selected stamp onto an appropriate place in the proof.

How to use it

- Click on the Add stamp icon in the Annotations section.
- Select the stamp you want to use. (The Approved stamp is usually available directly in the menu that appears).
- Click on the proof where you'd like the stamp to appear. (Where a proof is to be approved as it is, this would normally be on the first page).

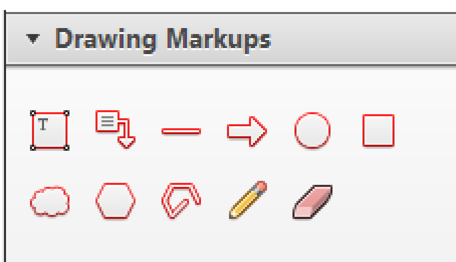

7. Drawing Markups Tools – for drawing shapes, lines and freeform annotations on proofs and commenting on these marks.

Allows shapes, lines and freeform annotations to be drawn on proofs and for comment to be made on these marks..

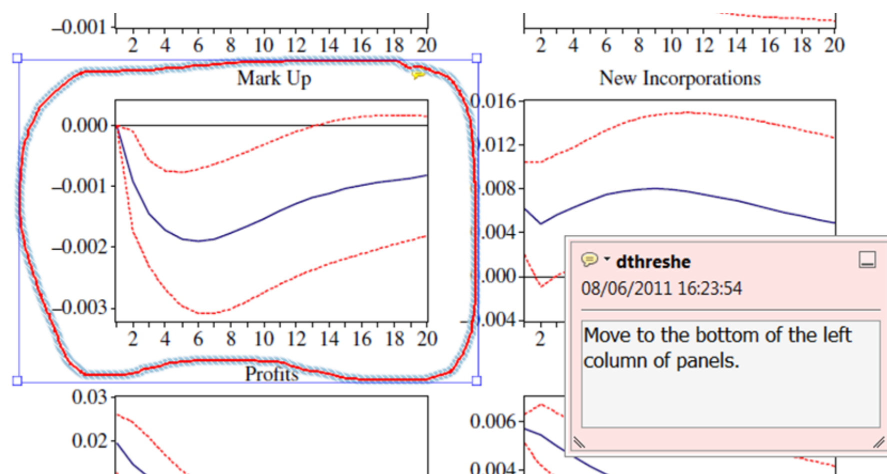

How to use it

- Click on one of the shapes in the Drawing Markups section.
- Click on the proof at the relevant point and draw the selected shape with the cursor.
- To add a comment to the drawn shape, move the cursor over the shape until an arrowhead appears.
- Double click on the shape and type any text in the red box that appears.

For further information on how to annotate proofs, click on the Help menu to reveal a list of further options: